materials

Article Paper

A Theoretical Treatment of THz Resonances in Semiconductor GaAs p-n Junctions

Mohsen Janipour *, I. Burc Misirlioglu and Kursat Sendur *

Faculty of Engineering and Natural Science, Sabanci University, Istanbul, 34956, Turkey; mjanipour@sabanciuniv.edu; burc@sabanciuniv.edu; sendur@sabanciuniv.edu

* Correspondence: mjanipour@sabanciuniv.edu; sendur@sabanciuniv.edu

Received: date; Accepted: date; Published: date

Abstract: Semiconductor heterostructures are suitable for the design and fabrication of THz plasmonic devices due to their matching carrier densities. The classical dispersion relations in the current literature are derived for metal plasmonic materials, such as gold and silver, for which a homogeneous dielectric function is valid. Penetration of the electric fields into semiconductors induces locally varying charge densities and a spatially varying dielectric function is expected. While such an occurrence renders tunable THz plasmonics a possibility, it is crucial to understand the conditions under which propagating resonant conditions for the carriers occur upon incidence of an electromagnetic radiation. In this manuscript, we derive a dispersion relation for a p-n heterojunction and apply the methodology to a GaAs p-n junction, a material of interest for optoelectronic devices. Considering symmetrically doped p- and n-type regions with equal width, effect of parameters, such as doping and voltage bias, on the dispersion curve of the p-n heterojunction are investigated. Keeping in sight the different effective masses and mobilities of the carriers, we were able to obtain the conditions that yield identical dielectric functions for the p- and n- regions. Our results indicate that the p-n GaAs system can sustain propagating resonances and can be used as a layered plasmonic waveguide. The conditions under which this is feasible fall in the frequency region between the transverse optical phonon resonance of GaAs and the traditional cut-off frequency of the diode waveguide. In addition, our results indicate when the excitation is slightly above phonon resonance frequency, the plasmon propagation attains low-loss characteristics. We also show that the existence or nonexistence of the depletion zone between the *p-* and *n-* interfaces allows certain plasmon modes to propagate, while others decay rapidly, pointing out the possibility for design of selective filters.

Keywords: Semiconductor plasmonics; semiconductor heterojunctions, plasmonic waveguide, p-n junction.

1. Introduction

The conductivity response of a junction formed between a semiconductor (SC) and a metal or a dielectric upon application of a voltage bias has been at the core of the semiconductor based solid state devices that led to the electronic revolution. The electronic characteristics of such a junction can be engineered via the choice of the materials and the doping on the SC side to achieve a desired response. Since the first appearance of semiconductor heterostructures, the sizes of devices have been considerably reduced to submicron scales owing to the advances in fabrication capabilities. In integrated circuits (IC), the main action of a semiconductor heterojunction is often whether to allow a current to pass or not, depending on the applied bias voltage and its sign. This is determined by the width of the depletion zone in a Schottky-type or pn- type junction. The former occurs upon contact of a metal with a semiconductor and the latter forms between dissimilar doped semiconductors.

Apart from their conductivity related applications, there emerged the idea to use semiconductor heterojunctions for optical manipulation, which goes back to the 1960s when a number of works analyzed electromagnetic wave transmission along a *pn*-junction at the millimeter scale and revealed some interesting optical physics in such systems[1,2]. Most notably, during the past decade, studies on the unique role of surface plasmon polaritons (SPPs) that allow propagation of light through subwavelength nanostructures has attained great interest in developing nano-photonic integrated circuits for a number of purposes[3,4]. The concept of SPPs coupled to specific excitation conditions has led to the development of various kinds of waveguides in the visible light regime[5–8]. Among these, due to their capability of photonic confinement, noble metallic based multilayer metal-insulator-metal (MIM) layers in the visible frequency regime has been widely studied by several researchers[9–11].

The interaction of light with the electrons of the noble metals at metal-dielectric interfaces of the MIM waveguides can result in much better SPP confinement due to the electromagnetic coupling of the localized free electron oscillations to the incoming excitation[10]. In addition to the noble metals, it has been shown by D. Y. Fedyanin *et al*.[12], A. V. Krasavin *et al*.[13] , R. Zektzer *et al*.[14], and O. Lotan *et al*.[15] that Cu, Si, and Al-based structures can also provide SPP guiding channels in the visible and IR regime. To achieve such plasmonic effects, other semiconductors like GaAs can also be considered in which free carriers of negative or positive signs with appropriate effective masses can populate either the conduction band or the valence band respectively via appropriate doping. GaAs has also been the choice for applications including manufacturing of microwave integrated circuits[16], infrared light emitting diodes[17], laser diodes[18], and solar cells[19]. In addition, plasmonic effects in GaAs can enable hybrid electro-optic/photonic integrated devices with high performance, easy-fabrication, and tunable properties with substantially high propagation length in comparison with the noble metals[20–24]. Consequently, applying the idea of doping to the multi-layered semiconductor heterostructure configuration, several applications like plasmonic optical modulators, waveguides, and meta-materials have been presumed for these novel photo-plasmonic devices in the IR and THz frequencies[25–30]. Luther *et al*.[31] and Williams *et al*.[32] have experimentally shown that similar tunable localized surface plasmon resonances (LSPR) can be achieved in doped semiconductor quantum dot structures for wave-guiding in the THz and IR regime[24–33]. The latter has also been shown for layered metal-dielectric-semiconductor and Schottky junctions can enable nanoscale SPP amplifiers using an electrical pump injected to the configuration[34–37]. Moreover, Fan *et al*.[38] showed that the electrically driven GaAs nanowire light sources can be coupled to plasmonic nano-strip waveguides. It has also been numerically shown that by tuning the positive voltage bias of a highly *pn*-doped diode a Y-junction optical switch can be obtained through the propagation of SPPs[39].

As semiconductors allow electric field penetration and possess carrier densities that can allow resonances, at least in theory, in the THz frequencies, we explore the characteristics of a *pn*-heterojunction for plasmonics. We demonstrate that, the existence/absence of the depletion zone at a *pn*-junction can act as a plasmonic filter for frequencies in the THz regime. The classical dispersion relations in the literature are already derived for metals, such as gold and silver, interfacing a dielectric for which a homogeneous dielectric function is valid. However, for semiconductor materials under an applied voltage, such as the p-n heterojunction, the dielectric constant varies as a function of coordinates resulting from the inhomogeneous electric field penetration. In this manuscript, we first derived a dispersion relation for the p-n heterojunction. Using these dispersion relations, we theoretically and numerically investigated the plasmonic wave-guiding mechanism of a GaAs based *pn*-junction at different doping densities. We carried out the analysis under various applied bias values. For the GaAs system, we show that when the excitation is slightly above phonon resonance frequencies, the plasmon propagation attains a low-loss characteristic, which is highly attractive for plasmon propagation applications. We also show that existence or nonexistence of the depletion zone between the *p*- and *n*- interfaces, controlled by applied bias, allows selective modes to propagate while others decay rapidly. One can design submicron devices around the concepts presented herein with plasmon-driven frequency selectivity in the optical regime.

2. Material Properties

GaAs is a III-V direct bandgap semiconductor with a zinc-blende crystal configuration[40]. Varga previously showed for GaAs that in the long-wavelength region the lattice vibrations and the conduction electrons have a combined contribution to its dielectric function[41]. Furthermore, several studies have investigated the interaction of bulk plasmons with optical phonons in the THz regime for the doped GaAs medium[24,42–44]. Although in the *p*-doped GaAs, the hole mobility is very low (i.e. $\mu_p = 400\mathrm{cm}^2.\mathrm{V}^{-1}.\mathrm{s}^{-1}$), the electron mobility in an *n*-doped GaAs medium is comparable (i.e. $\mu_n \le 8500\mathrm{cm}^2.\mathrm{V}^{-1}.\mathrm{s}^{-1}$) with those reported for graphene films (i.e. $\mu_n \approx 15000\mathrm{cm}^2.\mathrm{V}^{-1}.\mathrm{s}^{-1}$), that can in principle allow using of the GaAs medium as an optical waveguide in certain frequencies and doping values. GaAs system is attractive for the levels of doping that can be reached in this system without sacrificing lattice stability as well as the high mobility of the carriers among semiconductors including Si. Controlled doping combined with high carrier mobility could in principle allow THz resonances in a semiconductor and GaAs is an almost ideal platform material for this. MIM systems, on the other hand, are more suitable for visible and IR regions of the spectrum where the carrier mobilities and relaxation times can support resonances in the relevant spectral regime. The fact that carrier density can be controlled by an external DC bias in a semiconductor lattice provides the added functionality of resonance tunability that is otherwise absent in MIM structures.

In this section, the m_e is the electron mass, V_{bi} refers to the built-in potential, τ_j is the carrier relaxation time of the majority carriers in the relevant *p*- and *n*-doped regions, and γ_j is the damping frequency of the majority carriers in the relevant *p*- and *n*-doped regions and $\tau_j = 1/\gamma_j$. In general, for a bulk GaAs medium, one can represent the optical dielectric function as:

$$\varepsilon_{j-GaAs}(\omega) = \varepsilon_{\infty,GaAs}\left(1 - \frac{\omega_{pj}^2}{\omega(\omega + i\gamma_j)}\right) + \frac{(\varepsilon_{DC,GaAs} - \varepsilon_{\infty,GaAs})\cdot\omega_{TO}^2}{\omega_{TO}^2 - \omega^2 - i\omega\Gamma}, \quad (1)$$

where, $\varepsilon_{\infty,GaAs}$ and $\varepsilon_{DC,GaAs}$ are the high-frequency and static dielectric constant of GaAs, $j = p$, n, $\omega_{pj} = \sqrt{N_j \cdot e^2 / (\varepsilon_0 \varepsilon_{\infty,GaAs} m_j^*)}$, where e is the electron charge, N_j is the carrier concentration and γ_j represent the plasma and damping frequency of the majority carriers in the relevant *p*- and *n*-doped regions, respectively. The electron and hole effective masses in Eq. (1) are assumed as $m_n^* = 0.067\times m_e$, and $m_p^* = \left(\sqrt[3]{m_{lh}^2}+\sqrt[3]{m_{hh}^2}\right)/\left(\sqrt{m_{lh}}+\sqrt{m_{hh}}\right)$; with $m_{lh} = 0.53\times m_e$ and $m_{hh} = 0.08\times m_e$ as the light-hole and heavy-hole effective masses, respectively. We have also calculated the static conductivity of the bound holes and electrons in the doped GaAs using $\sigma = \sigma_{ps} + \sigma_{ns}$ where $\sigma_{js} = \pm e\cdot N_j \cdot \mu_j$ in which μ_j is the mobility of the hole and electron, respectively. In addition, to calculate the damping frequencies in Eq. (1), the carrier relaxation time in the doped GaAs is computed using the formula $\tau_j = m_j^*\sigma_{ps}/N_j e^2$ so that for the *p*- and *n*-doped regions and are approximately $\tau_p = 92\times 10^{-15}$ [sec] and $\tau_n = 324\times 10^{-15}$ [sec], which are much larger than the values of gold and silver (i.e., $\tau = 30-40$ [fsec]). In Eq. (1), ω_{TO} and Γ denote the transverse optical (TO) phonon resonance and damping phonon frequency, respectively, which are considered independent of the doping densities [45–47] and summarized in Table 1.

Table. 1. The optical parameters of GaAs medium used in Eq. (1)

$\varepsilon_{DC,GaAs}$	$\varepsilon_{\infty,GaAs}$	ω_{TO}(THz)	ω_{LO}(THz)	Γ(THz)
12.9	10.9	8	8.5	0.055

Figures [1(a), 1(c)] and Figs. [1(b), 1(d)], demonstrate the effect of p- and n-type dopants on real and imaginary parts of the dielectric function for $N_{p,n} = 10^{17}(\mathrm{cm}^{-3})$ [solid curve], $N_{p,n} = 10^{18}(\mathrm{cm}^{-3})$ [dashed curve], and $N_{p,n} = 10^{19}(\mathrm{cm}^{-3})$ [dashed-dotted curve], respectively. Please note that such doping levels have been reported for GaAs such as in the case of carrier mobility studies [48] as well as lattice stability of GaAs [49] and device design [50]. However, such aggressive atomic doping concentrations is still challenging to achieve in practical applications as the zinc blende GaAs has approximately 4.5 x1022 atoms/cm3. In Figs. [1(a)- 1(d)] it can be seen that the n-GaAs exhibits larger negative real and positive imaginary parts of the dielectric function in comparison to the p-GaAs. This is due to the lighter carrier effective mass in the conduction band than for holes in the valence band. For a constant doping density, by increasing the frequency, a much higher negative value of the real part and greater imaginary values can be obtained. Furthermore, in Figs. [1(a), 1(c)] and Figs. [1(b), 1(d)], it can be seen that although the phonon resonant frequency of the lattice is considered independent of the doping densities, the phonon-plasmon interactions are substantial for the relatively heavily doped cases. The real part of the dielectric function at frequencies before the TO phonon resonance frequency is strongly affected by the doping density that tends to have a more negative value. This property is significant in the n-doped GaAs in comparison to the p-GaAs. However, at certain frequencies it can be seen from Figs. [1(b), 1(d)] that the imaginary part of the dielectric function in the p-GaAs is approximately half of that of the n-GaAs. These optical properties make the doped GaAs an attractive candidate for novel plasmonic materials in the THz regime.

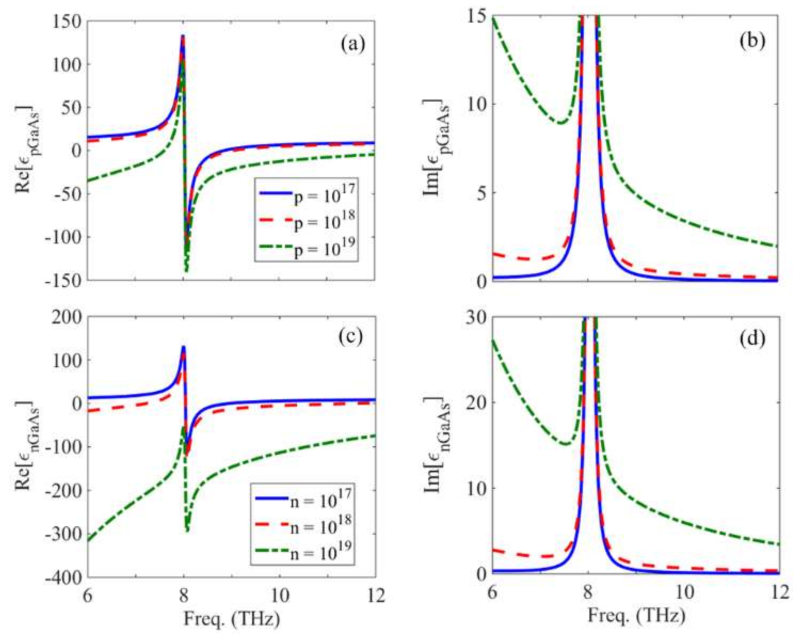

Figure 1. The spectral variation of the [(a), (c)] real and [(b), (d)] imaginary parts of the dielectric functions of the *p*- and *n*-GaAs for $N_{p,n} = 10^{17}(\mathrm{cm}^{-3})$ [solid curve], $N_{p,n} = 10^{18}(\mathrm{cm}^{-3})$ [dashed curve], and $N_{p,n} = 10^{19}(\mathrm{cm}^{-3})$ [dashed-dotted curve], respectively.

Keeping this behavior in mind, with the electronic features like charge distribution and band diagram of the semiconductor-metal interfaces, one can consider the layered plasmonic waveguide structures [51,52]. The plasmonic waveguide idea is centered around the concept of the gas oscillation model of free electrons in the visible regime where under phase-matched conditions the energy of the illuminating photons can be coupled to the free electrons of the noble metals at the metal-dielectric interface which can overcome the diffraction limits at nanoscale[11]. However, this behavior is a unique feature of the noble metals at visible light frequencies and at lower frequencies like gigahertz, terahertz, and FIR regime the plasmonic properties of the metals can no longer be tailored[24,39]. In the mid-IR regime, the optical properties of the GaAs medium can be analyzed via the Drude model, and the influence of the optical phonons is weak [53]. As we demonstrate in the following sections, an engineered *pn*-junction diode can provide alternative configurations owing to their inherent carrier transport characteristics at GHz and THz regimes where metals are no longer functional.

3. Dispersion relation for the p-n junction for inhomogeneous dielectric constant

To study the interaction of optical phonons with carriers and their resultant effect on the plasmon propagation in the GaAs pn-junction Interfacing metal electrodes (Figure 2), it is first worth to note that in Figs. 1(a-d), the pure plasmons caused by the Drude model (before ω_{TO}) are very lossy. Because of this property, we focus on frequency region around ω_{LO} which shows smaller imaginary part (low-loss) of the permittivity.

Figure 2(a) illustrates the schematic representation of the GaAs *pn*-junction under the external bias condition. First, we consider the symmetrical doped *p*- and *n*-doping regions with the equal width of d = 500 nm and $-V_{bi} \le V_A \le V_{bi}$. For the biased *pn*-diode, the width of the depletion region can be easily obtained by $w \approx \sqrt{\frac{2\varepsilon_{DC,GaAs}\varepsilon_0}{e}\sum_{j=p,n}(1/N_j)\cdot(V_{bi}-V_A)}$ such that $\varepsilon_{DC,GaAs}$ = 12.9 is the static dielectric constant of GaAs[52]. Considering the negative bias voltage values [i.e. $-V_{bi} \le V_A \le 0$]; formation of the depletion region is guaranteed while the positive voltage $V_A = +V_{bi}$ leads to zero depletion region width. Depletion zone's width depends mainly on two parameters; the bias voltage and the carrier density. This formula is valid for the static regime when under a fixed given bias and is considered to be insensitive to the electric field of the incident excitation.

According to Eq. (1), there is strong frequency dependency in the dielectric function of the doped GaAs bulk medium. As shown in Fig. 1(a), the *pn*-junction is bounded by ideal metal layers and is excited by a transverse magnetic (TM) mode in the *xz*-plane as a point source. The amplitude of the source is small enough that the width of the depletion region is not affected by the amplitude of the source (i.e. the dynamic field does not affect the static field caused by the applied bias). To compute the charge distribution, the top/bottom metal contacts are used to assign boundary conditions for solving the Poisson's equation from which one can extract the spatial charge distribution. Figure 2(b) shows the depletion region width as a function of bias and carrier density for symmetrical doping. The results in Fig. 2(b) suggest that the maximum depletion region width can be achieved for the low and moderately doping in the presence of a bias where $V_A = -V_{bi}$. For the heavily doping case a near-zero depletion region is created, i. e. depletion zone has negligible width (very small screening length). In Fig. 2(c) it can be seen that the depletion region is reduced to the half (i.e. maximum value of 100 nm) in the positive bias voltages. As it can be expected based on the equation of depletion zone, Fig. 2(c) shows that the minimum voltage i.e. zero provides the maximum depletion zone for this positive voltage range.

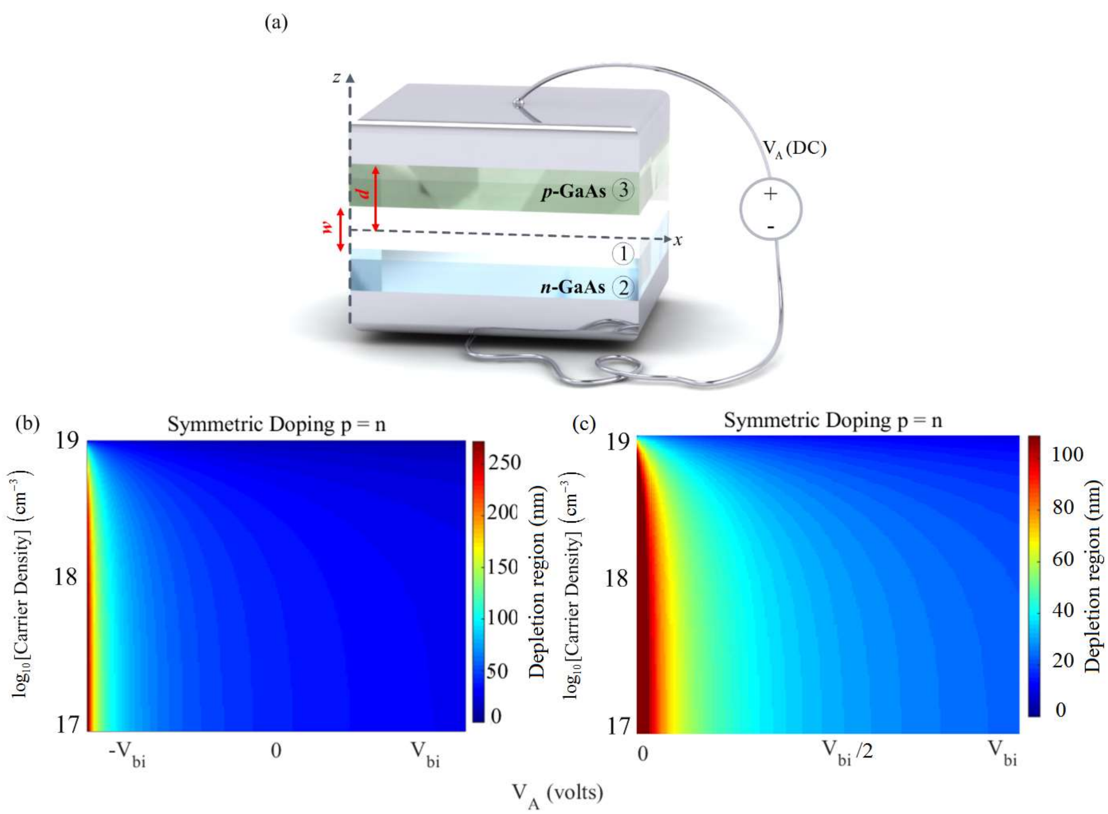

Figure 2. (a) Schematic representation of the considered structure. [(b), (c)] Variation of the depletion region width versus different carrier densities (in logarithmic scale) and applied bias voltage for symmetric doping case $-V_{bi} < V_A < V_{bi}$, and $0 < V_A < V_{bi}$, respectively.

To study a GaAs based semiconductor plasmonic waveguide, equipped with the generic dielectric functions derived in the previous section, we solve the Maxwell's equations and consider the TM mode excitation for the configuration shown in Fig. 2(a) to obtain the relevant dispersion relation. For $w/2 \le z \le d - w/2$:

$$\begin{aligned}
H_{y3}(\omega,V,z) &= e^{i\beta(\omega,V,z)x}\begin{Bmatrix} A_1\cos[k_3(\omega,V).(d-z)]+ \\ A_2\sin[k_3(\omega,V).(d-z)] \end{Bmatrix} \\
E_{x3}(\omega,V,z) &= \frac{-ik_3 e^{i\beta(\omega,V,z)x}}{\omega\varepsilon_0\varepsilon_3(\omega,V)}\begin{Bmatrix} A_1\sin[k_3(\omega,V).(d-z)]- \\ A_2\cos[k_3(\omega,V).(d-z)] \end{Bmatrix} \\
E_{z3}(\omega,V,z) &= \frac{-\beta e^{i\beta(\omega,V,z)x}}{\omega\varepsilon_0\varepsilon_3(\omega,V)}\begin{Bmatrix} A_1\cos[k_3(\omega,V).(d-z)]+ \\ A_2\sin[k_3(\omega,V).(d-z)] \end{Bmatrix}
\end{aligned} \tag{2}$$

and for $-w/2 \le z \le w/2$:

$$\begin{aligned}
H_{y1}(\omega,V,z) &= e^{i\beta(\omega,V,z)x}\begin{Bmatrix} C_1\cos[k_1(\omega,V).(d-z)]+ \\ C_2\cos[k_1(\omega,V).(d+z)] \end{Bmatrix} \\
E_{x1}(\omega,V,z) &= \frac{-ik_1 e^{i\beta(\omega,V,z)x}}{\omega\varepsilon_0\varepsilon_1}\begin{Bmatrix} C_1\sin[k_1(\omega,V).(d-z)]- \\ C_2\sin[k_1(\omega,V).(d+z)] \end{Bmatrix} \\
E_{z1}(\omega,V,z) &= \frac{-\beta(\omega,V,z) e^{i\beta(\omega,V,z)x}}{\omega\varepsilon_0\varepsilon_1}\begin{Bmatrix} C_1\cos[k_1(\omega,V).(d-z)]+ \\ C_2\cos[k_1(\omega,V).(d+z)] \end{Bmatrix}
\end{aligned} \tag{3}$$

and for $-w/2 \le z \le w/2 - d$:

$$\begin{aligned}
H_{y2}(\omega,V,z) &= e^{i\beta(\omega,V,z)x}\begin{Bmatrix} B_1\cos[k_2(\omega,V).(d+z)]+ \\ B_2\sin[k_2(\omega,V).(d+z)] \end{Bmatrix} \\
E_{x2}(\omega,V,z) &= \frac{-ik_2 e^{i\beta(\omega,V,z)x}}{\omega\varepsilon_0\varepsilon_2}\begin{Bmatrix} -B_1\sin[k_2(\omega,V).(d+z)]+ \\ B_2\cos[k_2(\omega,V).(d+z)] \end{Bmatrix} \\
E_{z2}(\omega,V,z) &= \frac{-\beta(\omega,V,z) e^{i\beta(\omega,V,z)x}}{\omega\varepsilon_0\varepsilon_2}\begin{Bmatrix} B_1\cos[k_2(\omega,V).(d+z)]+ \\ B_2\sin[k_2(\omega,V).(d+z)] \end{Bmatrix}
\end{aligned} \tag{4}$$

where $k_j(\omega,V) = \sqrt{\beta^2(\omega,V) - k_0^2\varepsilon_j(\omega)}$ with j = 1, 2, 3. Since the tangential electric field component at perfect electric conductor interfaces (i.e., $z = \pm d$) should be equal to zero, leads to $A_2 = B_2 = 0$. In addition, using the continuity of $H_{yi}(\omega,V,z)$ and $E_{xi}(\omega,V,z)$ field components at $z = \pm w/2$ boundaries, may result the following SPP dispersion relation:

$$\begin{aligned}
&\frac{\cos[k_1(\omega,V).(d-w/2)]}{\cos[k_1(\omega,V).(d+w/2)]} = \\
&\pm\sqrt{\frac{M_2(\omega,V).\tan[k_1(\omega,V).(d+w/2)] + \tan[k_2(\omega,V).(d-w/2)]}{M_2(\omega,V).\tan[k_1(\omega,V).(d-w/2)] - \tan[k_2(\omega,V).(d-w/2)]}} \times \\
&\sqrt{\frac{M_3(\omega,V).\tan[k_1(\omega,V).(d+w/2)] + \tan[k_3(\omega,V).(d-w/2)]}{M_3(\omega,V).\tan[k_1(\omega,V).(d-w/2)] - \tan[k_3(\omega,V).(d-w/2)]}},
\end{aligned} \tag{5}$$

where $k_j(\omega,V)=\sqrt{\beta^2(\omega,V)-k_0^2\varepsilon_j(\omega)}$ with j = 1-3, and $M_{2,3}(\omega,V)=k_1(\omega,V)/k_{2,3}(\omega,V)\times\varepsilon_{2,3}(\omega)/\varepsilon_1(\omega)$.

According to Eq. (5), if we insert $w=2d$ i.e., the entire space between the metallic plates becomes intrinsic GaAs and no electromagnetic mode can propagate inside the diode because Eq. (5) has no solution. Moreover, according to Eq. (5), it can be seen that, unlike the MIM waveguide structures, in the *pn*-junction diode only the even plasmonic modes can be excited due to the presence of the cosine function. In this manuscript, the existence and properties of the propagating modes for the GaAs systems are discussed. Once the existence and properties of these modes are established, the excitation of these modes can be achieved using traditional techniques, such as Kretschmann configuration [54] or end-fire coupling [55]. In this regard, we expect that the excitation of the modes of the proposed layered GaAs system will be quite similar to a traditional metal-insulator-metal (MIM) system.

4. Results

4.1. Symmetric Doping Densities

In addition to the theoretical dispersion relations given in the previous section, we carried out numerical simulations to obtain the dispersion results that are provided in Fig. 3(a)-(c). For the numerical simulation of the proposed heterostructure waveguide, a full-wave finite-difference time-domain (FDTD) method has been used in this manuscript. A uniform discretization of the system with unit cell dimensions of 10 nm is used throughout the computational domain as no further mesh refinement method was needed throughout the computation. The computational grid has a finite size of $60\times1\,(\mu\mathrm{m})^2$ with boundary conditions corresponding to uniaxial anisotropic perfectly matched layers (PMLs) where 16 PMLs were used to render absorbing boundary conditions. The computation time is set as t = 20000 fs with time step Δt = 0.87 fs which satisfies the Cournat-Friedrichs-Lewy (CFL) stability factor condition of $\Delta t\le1/c\sqrt{\Delta x^{-2}+\Delta y^{-2}+\Delta z^{-2}}$ in which c is the speed of light in free space. The waveguide is excited with a broadband dipolar point source as an oscillating electric dipole along direction of wave propagation (x-axis) at f_0 = 6.5 THz with the pulse length of 166 fs and spectral bandwidth of 11 THz. Figures 3(a)-3(c) show the normalized dispersion curve peaks of the *pn*-junction diode obtained from the finite-difference time-domain (FDTD) simulations for the carrier densities of (a) $N_{p,n}=10^{17}\,(\mathrm{cm}^{-3})$, (b) $N_{p,n}=10^{18}\,(\mathrm{cm}^{-3})$, and (c) $N_{p,n}=10^{19}\,(\mathrm{cm}^{-3})$ in the case of symmetrical doping, and external bias voltages of $V_A=+V_{bi}$ (circles), and $-V_{bi}<V_A<0$ (crosses), respectively. Our simulations show that there is no difference in the dispersion curves for negative voltages (i.e. -V_bi<V_A<0).

As shown in Figs. 3(a)-3(c), the asymptotic frequencies of the low-doping density, such as $N_{p,n}=10^{17}\,(\mathrm{cm}^{-3})$ are displayed for positive, and negative bias voltages which correspond to the sitation where depletion zone width for 0 and negative bias smaller than V_{bi} does not have notable difference. In other words, in this case relatively small plasmon frequency intervals of f = 2.57 THz to 2.95 THz and f = 8.76 to 8.92 THz exist between zero, and non-zero depletion width when $V_A=+V_{bi}$ and $-V_{bi}<V_A<0$, respectively. According to Figs. 3(b) and 3(c), for the doping densities of

$N_{p,n} = 10^{18}(\mathrm{cm}^{-3})$, and $N_{p,n} = 10^{19}(\mathrm{cm}^{-3})$ the asymptotes can cover wider frequency bands especially in the lower frequencies. This implies a wider spectral regime of propagation. For example in the case of $N_{p,n} = 10^{18}(\mathrm{cm}^{-3})$ it is obvious that the asymptotes can cover the frequencies between *f* = 3.71 to 5.89 THz and *f* = 9.05 to 9.66 THz for $-V_{bi} < V_A < 0$, while for $V_A = +V_{bi}$ a wider band between *f* = 1.27 THz to 6.06 THz and *f* = 8.97 THz to 9.34 THz is covered, respectively.

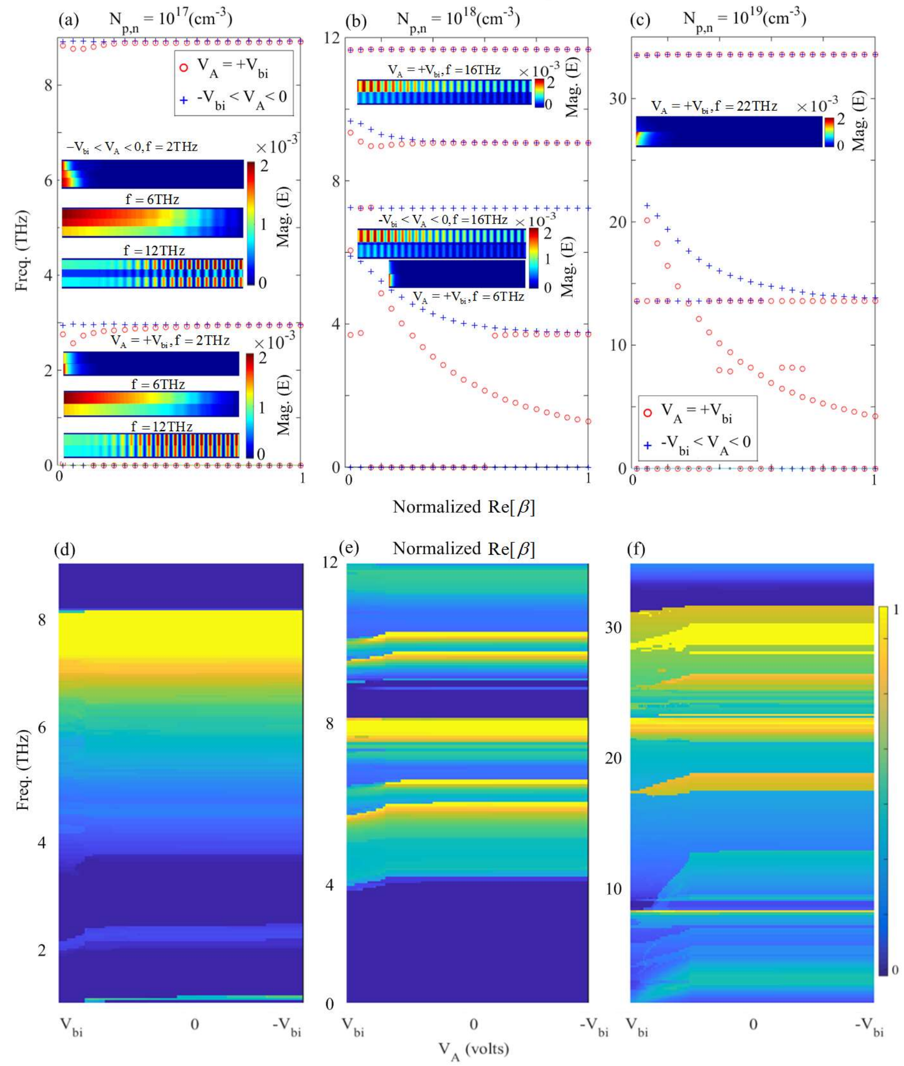

Figure 3. Dispersion curve peaks of the *pn*-junction with applied bias voltages of $V_A = +V_{bi}$ (circles), and $-V_{bi} < V_A < 0$ (crosses), for carrier densities (a) $N_{p,n} = 10^{17}(\mathrm{cm}^{-3})$, (b) $N_{p,n} = 10^{18}(\mathrm{cm}^{-3})$, and (c) $N_{p,n} = 10^{19}(\mathrm{cm}^{-3})$ symmetric doping, respectively. The relevant two dimensional variation of the normalized dispersion curve obtained theoretically using equation (3) for (d) $N_{p,n} = 10^{17}(\mathrm{cm}^{-3})$, (e) $N_{p,n} = 10^{18}(\mathrm{cm}^{-3})$, and (f) $N_{p,n} = 10^{19}(\mathrm{cm}^{-3})$ symmetric doping, respectively.

Non-plasmonic modes emerge beyond $f \approx 43\mathrm{THz}$ on the left side of the light line due to the cut-off frequencies of the metallic waveguide-like behavior of the diode. Therefore, we concentrate on the lower frequencies to investigate the depletion zone dependent effects under negative and positive bias voltages.

Figure 3(c) shows that for $N_{p,n} = 10^{19}(\mathrm{cm}^{-3})$ the asymptotes emerge at higher frequencies due to greater plasmon frequency resulted from higher doping values. The asymptotes cover wider frequency band between *f* = 4.21 THz to 20.13 THz for $V_A = +V_{bi}$ in comparison with *f* = 13.6 THz to 21.33 THz band for $-V_{bi} < V_A < 0$. This feature is useful for filtering purposes in the nano-photonics integrated circuits at the THz regime. For the asymptotic case with $w = 0$ occurring under $V_A = +V_{bi}$, theoretically two conditions can exist: 1) $\tan(k_1 d) = 0$, and 2) a transcendental equation of $(k_3/\varepsilon_3)\times\tan(k_3 d) + (k_2/\varepsilon_2)\times\tan(k_2 d) = 0$ condition. Since, under this voltage, there is no depletion region the first condition may not be satisfied and just the second condition can exist at some frequencies. To study the p-n junction waveguide theoretically, we plot the solution of Eq. (3) versus the bias voltage. Figures 3(d)-3(f) illustrate the normalized dispersion curve using an interior, subspace conjugate gradient method[56] obtained for (d) $N_{p,n} = 10^{17}(\mathrm{cm}^{-3})$, (e) $N_{p,n} = 10^{18}(\mathrm{cm}^{-3})$, and (f) $N_{p,n} = 10^{19}(\mathrm{cm}^{-3})$, respectively. It can be seen that as mentioned earlier using the simulation results [Figs. 3(a)-3(c)], the dispersion curve is constant for whole of the voltage region that $w \neq 0$ i.e. $-V_{bi} < V_A < 0$, and is different for the case that $w = 0$ i.e. for $V_A = +V_{bi}$. Although there are some frequency deviations and ripples in the dispersion curves, for the high-doping values [Figs. 3(e), and 3(f)], the results support a notable wave guiding trend in the *pn*-junction. Therefore, based on the simulation and theoretical results shown in Figs. 3(a)-3(f), it can be stated that unlike the MIM waveguide structures wherein the thickness of the insulator layer determines the propagation wavelength of the wave, for the diode waveguide; existence or lack of the depletion zone can change the frequency of the propagating plasmon wave. The results in Fig. 3 suggest that increasing the doping density results in the blue-shift of the asymptotic plasmonic frequencies. The insets of Figs. 3(a)-3(c) show the distribution of absolute value of the E_x component of the electric field inside the waveguide. It can be seen that for example in the case of $N_{p,n} = 10^{17}(\mathrm{cm}^{-3})$ although the dispersion curve does not represent an asymptotic frequency at *f* = 2 THz, the imaginary part of the individual dielectric functions are such high [see Figs. 1(a)-1(d)] that the wave cannot propagate inside the waveguide and gets rapidly damped.

For the frequency bands between the asymptotic frequencies and the first traditional cut-off frequency of the metallic waveguide, i.e. *f* = 6 THz and 12 THz respectively, the wave can much more easily propagate due to lower propagation loss of the doped mediums and near-zero-epsilon conditions [see Figs. 1(a)-1(d)]. Similarly, the same situation governs the wave propagation for $N_{p,n} = 10^{18}(\mathrm{cm}^{-3})$; at *f* = 6 THz and 16 THz; and $N_{p,n} = 10^{19}(\mathrm{cm}^{-3})$ at *f* = 22 THz in Figs. 6(b) and 6(c), respectively.

Based on the insets of Figs. 3(a)-3(c), it is found that, due to the different dispersion properties of the *p*- and *n*-doped regions at a certain frequency, the electric field distribution in each of the doped regions are different as expected. Therefore, the electric field at a given frequency of the excitation experiences various phase differences in each of the regions. Figures 4(a)-4(f) show the normalized amplitude and the relevant phase variations of the E_x component of the electric field along *z*-

direction for $V_A = +V_{bi}$ (solid-curves) and $-V_{bi} < V_A < 0$ (dashed-curves) and $N_{p,n} = 10^{17}(\mathrm{cm}^{-3})$ [(a), (b)] at *f* = 2 THz (blue-curve), 6 THz (red-curve), and 12 THz (green-curve); $N_{p,n} = 10^{18}(\mathrm{cm}^{-3})$ [(c), (d)] at *f* = 2 THz (blue-curve), 6 THz (red-curve), and 16 THz (green-curve); and $N_{p,n} = 10^{19}(\mathrm{cm}^{-3})$ [(e), (f)] at *f* = 22 THz (blue-curve), 35 THz (red-curve), respectively. In Figs. 4(a)-4(f), the regions 1, 2, and 3 correspond to the depletion region, *n*-doped region, and *p*-doped region, respectively [see Fig. 2(a)].

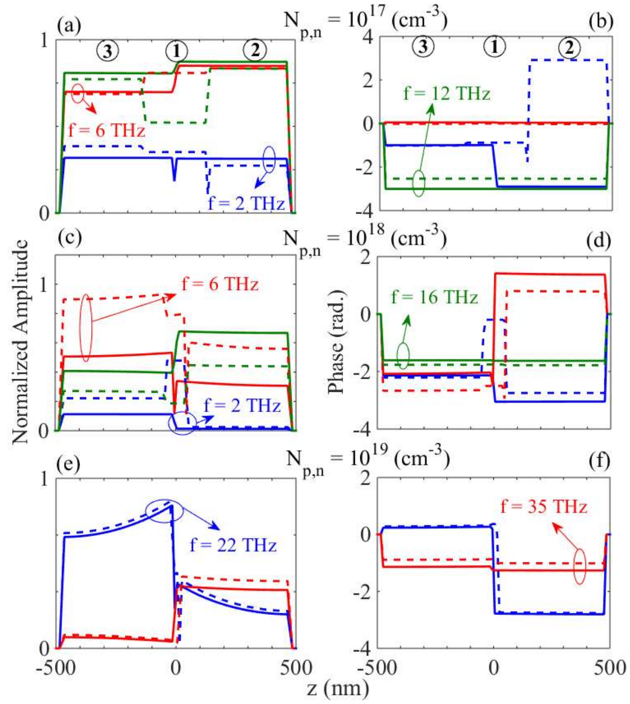

Figure 4. The normalized electric field amplitude and phase variation inside the *pn*-junction waveguide for the individual $V_A = +V_{bi}$ (solid-curves), and $V_A = -V_{bi}$ (dashed-curves) [(a), (b)] $N_{p,n} = 10^{17}(\mathrm{cm}^{-3})$ at *f* = 2 THz (blue-line), 6 THz (red-line), and 12THz (green-line); [(c), (d)] $N_{p,n} = 10^{18}(\mathrm{cm}^{-3})$ at *f* = 2 THz (blue-line), 6 THz (red-line), and 16THz (green-line); [(e), (f)] $N_{p,n} = 10^{19}(\mathrm{cm}^{-3})$ at *f* = 22 THz (blue-line), 35 THz (red-line), respectively.

It should be noted that Figs. 1(a)-1(d) depict the optical properties of the bulk GaAs medium without any surface or boundary effects unlike the hetereostructure investigated in this work. Fig.1 serves as a basis for the calculations undertaken for the finite heterostructure. The fields plotted in Figs. 4(a)-4(f) are related to the waveguide structure where the boundary conditions and surface effects have been considered. In Figs. 4(a) and 4(b) for $N_{p,n} = 10^{17}(\mathrm{cm}^{-3})$ it can be seen that at *f* = 2 THz although the amplitudes are approximately equal, the phase difference of the electric fields in 3 and 2 mediums for the positive and negative biases are between $\pi/2$ (rad.) and π (rad.), however, for the positive bias voltage at *f* = 6 THz and 12 THz a zero phase difference and approximately equal amplitudes are obtained, preventing destructive interference effects and the propagating solutions are damped at larger distances. Similarly, for $N_{p,n} = 10^{18}(\mathrm{cm}^{-3})$ using Figs. 4(c) and 4(d) the phase difference of the propagating E_x component in 1, 2 and 3 mediums at f = 16 THz is equal to zero, whereas, the amplitudes are slightly different especially in the case of the negative voltage. It seems that this issue arises due to the smaller difference of the imaginary parts of the semiconductor mediums in the case of $N_{p,n} = 10^{17}\,(\mathrm{cm}^{-3})$ and $N_{p,n} = 10^{18}\,(\mathrm{cm}^{-3})$ and at frequencies greater than ω_{TO}. On the other hand, this behavior is not observed for $N_{p,n} = 10^{19}\,(\mathrm{cm}^{-3})$ [see Figs. 4(e) and 4(f)].

4.2. Asymmetric Doping Densities

In this section, the optical properties of the waveguide under asymmetric carrier concentration are discussed. Here we show that the decoherency effects due to the difference in the effective masses of electrons and holes in the n- and p-doped regions are further enhanced due to asymmetrical doping. In addition to the differences between the plasmon frequencies, since the electron and hole mobilities in the *p*- and *n*-doped regions are considerably different, the carrier relaxation time and hence the collision rate of these regions also differ. These effects eventually lead to different dielectric functions of the doped mediums, which in turn, disturbs the propagated field inside the *pn*-junction waveguide. Thus, in order to avoid such effects, the equal dielectric function condition of the *p*- and *n*-GaAs based on Eq. (1); i.e. $\mathrm{Re}[\varepsilon_{p-GaAs}(\omega)] = \mathrm{Re}[\varepsilon_{n-GaAs}(\omega)]$ needs to be achieved:

$$\begin{pmatrix} N_p \\ N_n \end{pmatrix} = \begin{pmatrix} N_n \\ N_p \end{pmatrix} \times \begin{pmatrix} m_p^* / m_n^* \\ m_n^* / m_p^* \end{pmatrix} \times \left\{ \begin{array}{c} \left(\dfrac{\omega^2 + \dfrac{e^2}{4\pi^2 \cdot \mu_p^2 \cdot m_p^*}}{\omega^2 + \dfrac{e^2}{4\pi^2 \cdot \mu_n^2 \cdot m_n^*}} \right) \\ \left(\dfrac{\omega^2 + \dfrac{e^2}{4\pi^2 \cdot \mu_n^2 \cdot m_n^*}}{\omega^2 + \dfrac{e^2}{4\pi^2 \cdot \mu_p^2 \cdot m_p^*}} \right) \end{array} \right\} \tag{6}$$

Since we are interested in small amplitudes of the excitation field which does not change the width of the depletion region, we concentrate on the carrier densities in the static regime:

$$\begin{pmatrix} N_p \\ N_n \end{pmatrix} = \begin{pmatrix} N_n \\ N_p \end{pmatrix} \cdot \begin{pmatrix} m_n^* / m_p^* \\ m_p^* / m_n^* \end{pmatrix} \cdot \begin{pmatrix} \mu_n / \mu_p \\ \mu_p / \mu_n \end{pmatrix}^2 \tag{7}$$

In Eq. (7) the carrier density relation, which results in the same relative permittivity in the static situation, strongly depends on the ratio of the effective masses and square of ratios of the electron and hole mobilities, respectively. To achieve an equal dielectric function in both regions, the n-region doping values of $N_n = 10^{17}(\mathrm{cm}^{-3})$, $N_n = 10^{18}(\mathrm{cm}^{-3})$, and $N_n = 10^{19}(\mathrm{cm}^{-3})$ should correspond to a p-region doping ratio of $N_p = 7.5\times10^{18}(\mathrm{cm}^{-3})$, $N_p = 7.5\times10^{19}(\mathrm{cm}^{-3})$, and $N_p = 7.5\times10^{20}(\mathrm{cm}^{-3})$, for weak, moderate and heavy doping respectively.

Figures 5(a)-5(c) demonstrate the dispersion curve peaks for the *pn*-junction waveguide with $N_n = 10^{17}(\mathrm{cm}^{-3})$, $N_p = 7.5\times10^{18}\ (\mathrm{cm}^{-3})$ [Fig. 5(a)]; $N_n = 10^{18}\ (\mathrm{cm}^{-3})$ and $N_p = 7.5\times10^{19}\ (\mathrm{cm}^{-3})$ [Fig. 5(b)],

$N_n = 10^{19}$ (cm^{-3}) and $N_p = 7.5\times10^{20}$ (cm^{-3}) [Fig. 5(c)] doping densities, for $V_A = +V_{bi}$ (circles) and $-V_{bi} < V_A < 0$ (crosses), respectively. According to Figs. 5(a)-5(c), for the case of the positive voltage, the asymptotic frequencies are negligibly blue-shifted in comparison to the symmetric doping case; for example for $N_n = 10^{17}$(cm^{-3}), $N_p = 7.5\times10^{18}$(cm^{-3}) we have the asymptotes of *f* = 2.98 THz and 8.97 THz which occurred at *f* = 2.96 THz and 8.91 THz for $N_{p,n} = 10^{17}$(cm^{-3}) and also we obtain *f* = 7.27 THz and 11.69 THz for $N_n = 10^{18}$(cm^{-3}) and $N_p = 7.5\times10^{19}$(cm^{-3}) while we see asymptotes at *f* = 7.24 THz and 11.65 THz for $N_{p,n} = 10^{18}$(cm^{-3}) symmetric doping densities, respectively.

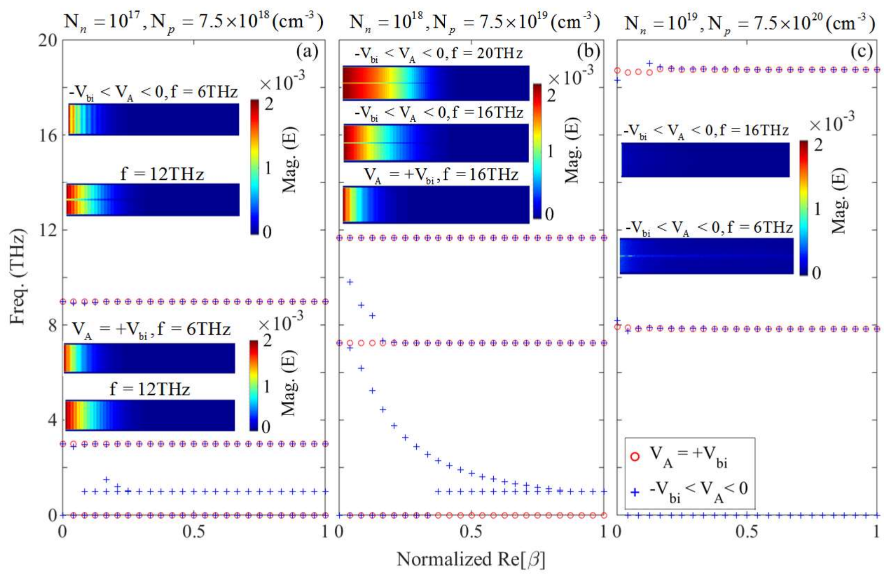

Figure 5. Dispersion curve peaks of the pn-junction with applied bias voltages of $V_A = +V_{bi}$ (circles), and $-V_{bi} < V_A < 0$ (crosses) achieved from the simulations, for carrier densities (a) $N_n = 10^{17}$(cm^{-3}) and $N_p = 7.5\times10^{18}$(cm^{-3}), (b) $N_n = 10^{18}$(cm^{-3}) and $N_p = 7.5\times10^{19}$(cm^{-3}), and (c) $N_n = 10^{19}$(cm^{-3}) and $N_p = 7.5\times10^{20}$(cm^{-3}) doping densities, respectively. The insets show the amplitude of E_x component at *f* = 6 THz and 12 THz for $N_n = 10^{17}$(cm^{-3}) and $N_p = 7.5\times10^{18}$(cm^{-3}), at *f* = 16 THz and 20 THz for $N_n = 10^{18}$(cm^{-3}) and $N_p = 7.5\times10^{19}$(cm^{-3}), and at *f* = 6 THz and 16 THz for $N_n = 10^{19}$(cm^{-3}) and $N_p = 7.5\times10^{20}$(cm^{-3}), respectively.

Furthermore, based on Figs. 5(a)-5(c) it is obvious that in the case of applied negative bias, another asymptotic frequency at *f* = 1 THz originates for $N_n = 10^{17}$ (cm^{-3}), $N_p = 7.5\times10^{18}$ (cm^{-3}) and also for $N_n = 10^{18}$ (cm^{-3}) and $N_p = 7.5\times10^{19}$ (cm^{-3}). Unlike the symmetric doping densities, for the asymmetric case, the positive voltage cannot support a substantial wide region of plasmonic asymptotic frequencies. For $N_n = 10^{18}$ (cm^{-3}) and $N_p = 7.5\times10^{19}$ (cm^{-3}) with negative voltages we can achieve an ultra-wide asymptotic frequency band of 8.82 THz between $f = 1$ THz and 9.82 THz. Although, in the asymmetric doping densities the electric field inside the *pn*-junction waveguide is uniform and in-phase along the *z*-axis in both the *p*- and *n*-doped medium, the insets of the Figs. 5(a)-5(c) reveal that the electromagnetic field at a certain frequency cannot propagate as easily as it does in the case of the asymmetric doping at the relevant frequency.

5. Conclusion

In this work, we derived a dispersion relation for the p-n heterojunction and applied the resulting relations to a GaAs based p-n junction using the material constants and band parameters from existing literature. With the use of the dispersion curves and carrying out numerical simulations, we showed that better tunability can be achieved at frequencies between the TO phonon resonance frequency and the first cut-off frequency of the GaAs filled metallic waveguide. We theoretically and numerically demonstrate that the pn- junction waveguide, unlike the MIM waveguides, supports both plasmonic asymptotic, and cut-off frequencies of the traditional waveguide but in the THz regime. We also show that highly asymmetric doping levels may cause phase shifts of the propagating plasmon waves in the n- and p-doped regions that lead to loss of coherency of the propagating waves. Our findings point out the way doped pn junctions or similar heterostructures can be tailored for a variety of tunable optoelectronic applications. Such features of pn-junction waveguides hold promise for low-loss, wide bandwidth optoelectronic applications in the THz spectrum and can act as efficient interfaces between ICs and optics.

References

[1] Yariv A and Leite R C C 1963 Dielectric-waveguide mode of light propagation in p-n junctions *Appl. Phys. Lett.* **2** 55–7

[2] Bond W L, Cohen B G, Leite R C C and Yariv A 1963 Observation of the dielectric-waveguide mode of light propagation in p-n junctions *Appl. Phys. Lett.* **2** 57–9

[3] Wei H, Zhang S, Tian X and Xu H 2013 Highly tunable propagating surface plasmons on supported silver nanowires. *Proc. Natl. Acad. Sci. U. S. A.* **110** 4494–9

[4] Zhang S, Wei H, Bao K, Håkanson U, Halas N J, Nordlander P and Xu H 2011 Chiral Surface Plasmon Polaritons on Metallic Nanowires *Phys. Rev. Lett.* **107** 096801

[5] Holmgaard T, Chen Z, Bozhevolnyi S I, Markey L, Dereux A, Krasavin A V. and Zayats A V. 2009 Wavelength selection by dielectric-loaded plasmonic components *Appl. Phys. Lett.* **94** 051111

[6] Chen Z, Holmgaard T, Bozhevolnyi S I, Krasavin A V., Zayats A V., Markey L and Dereux A 2009 Wavelength-selective directional coupling with dielectric-loaded plasmonic waveguides *Opt. Lett.* **34** 310

[7] Bian Y and Gong Q 2014 Tuning the hybridization of plasmonic and coupled dielectric nanowire modes for high-performance optical waveguiding at sub-diffraction-limited scale *Sci. Rep.* **4** 6617

[8] Holmgaard T, Chen Z, Bozhevolnyi S I, Markey L, Dereux A, Krasavin A V. and Zayats A V. 2008 Bend- and splitting loss of dielectric-loaded surface plasmon-polariton waveguides *Opt. Express* **16** 13585

[9] Burke J J, Stegeman G I and Tamir T 1986 Surface-polariton-like waves guided by thin, lossy metal films *Phys. Rev. B* **33** 5186–201
[10] Dionne J A, Sweatlock L A, Atwater H A and Polman A 2006 Plasmon slot waveguides: Towards chip-scale propagation with subwavelength-scale localization *Phys. Rev. B* **73** 035407
[11] Maier S A 2007 *Plasmonics: fundamentals and applications* (Springer US)
[12] Fedyanin D Y, Yakubovsky D I, Kirtaev R V. and Volkov V S 2016 Ultralow-Loss CMOS Copper Plasmonic Waveguides *Nano Lett.* **16** 362–6
[13] Krasavin A V. and Zayats A V. 2010 Silicon-based plasmonic waveguides *Opt. Express* **18** 11791
[14] Zektzer R, Desiatov B, Mazurski N, Bozhevolnyi S I and Levy U 2014 Experimental demonstration of CMOS-compatible long-range dielectric-loaded surface plasmon-polariton waveguides (LR-DLSPPWs) *Opt. Express* **22** 22009
[15] Lotan O, Smith C L C, Bar-David J, Mortensen N A, Kristensen A and Levy U 2016 Propagation of Channel Plasmons at the Visible Regime in Aluminum V-Groove Waveguides *ACS Photonics* **3** 2150–7
[16] Larson L E, Hackett R H and Lohr R F 1991 Microactuators for GaAs-based microwave integrated circuits *Int. Conf. Solid-State Sensors and Actuators* (IEEE) pp 743–6
[17] Yeh H-J J and Smith J S 1994 Fluidic self-assembly for the integration of GaAs light-emitting diodes on Si substrates *IEEE Photonics Technol. Lett.* **6** 706–8
[18] Dupuis R D, Dapkus P D, Holonyak N, Rezek E A and Chin R 1978 Room-temperature laser operation of quantum-well $Ga_{(1-x)}Al_{x}As$-GaAs laser diodes grown by metalorganic chemical vapor deposition *Appl. Phys. Lett.* **32** 295–7
[19] Yablonovitch E, Miller O D and Kurtz S R 2012 The opto-electronic physics that broke the efficiency limit in solar cells *38th IEEE Photovol. Spec. Conf.* (IEEE) pp 001556–9
[20] Pitilakis A and Kriezis E E 2013 Highly nonlinear hybrid silicon-plasmonic waveguides: analysis and optimization *J. Opt. Soc. Am. B* **30** 1954
[21] Chou L-W, Shin N, Sivaram S V. and Filler M A 2012 Tunable Mid-Infrared Localized Surface Plasmon Resonances in Silicon Nanowires *J. Am. Chem. Soc.* **134** 16155–8
[22] Law S, Podolskiy V and Wasserman D 2013 Towards nano-scale photonics with micro-scale photons: the opportunities and challenges of mid-infrared plasmonics *Nanophotonics* **2** 103–30
[23] Kinsey N, Ferrera M, Shalaev V M and Boltasseva A 2015 Examining nanophotonics for integrated hybrid systems: a review of plasmonic interconnects and modulators using traditional and alternative materials [Invited] *J. Opt. Soc. Am. B* **32** 121
[24] Janipour M, Misirlioglu I B and Sendur K 2016 Tunable Surface Plasmon and Phonon Polariton Interactions for Moderately Doped Semiconductor Surfaces *Sci. Rep.* **6** 34071
[25] Qi Z, Hu G, Li L, Yun B, Zhang R and Cui Y 2016 Design and Analysis of a Compact SOI-Based Aluminum/Highly Doped p-Type Silicon Hybrid Plasmonic Modulator *IEEE Photonics J.* **8** 1–11
[26] Rodríguez-Fortuño F J, Espinosa-Soria A and Martínez A 2016 Exploiting metamaterials, plasmonics and nanoantennas concepts in silicon photonics *J. Opt.* **18** 123001
[27] Law S, Adams D C, Taylor A M and Wasserman D 2012 Mid-infrared designer metals *Opt. Express* **20** 12155
[28] Law S, Roberts C, Kilpatrick T, Yu L, Ribaudo T, Shaner E A, Podolskiy V and Wasserman D

2014 All-Semiconductor Negative-Index Plasmonic Absorbers *Phys. Rev. Lett.* **112** 017401

[29] N'Tsame Guilengui V, Cerutti L, Rodriguez J-B, Tournié E and Taliercio T 2012 Localized surface plasmon resonances in highly doped semiconductors nanostructures *Appl. Phys. Lett.* **101** 161113

[30] Jun Y C and Brener I 2012 Electrically tunable infrared metamaterials based on depletion-type semiconductor devices *J. Opt.* **14** 114013

[31] Luther J M, Jain P K, Ewers T and Alivisatos A P 2011 Localized surface plasmon resonances arising from free carriers in doped quantum dots *Nat. Mater.* **10** 361–6

[32] Williams C R, Andrews S R, Maier S A, Fernández-Domínguez A I, Martín-Moreno L and García-Vidal F J 2008 Highly confined guiding of terahertz surface plasmon polaritons on structured metal surfaces *Nat. Photonics* **2** 175–9

[33] Goykhman I, Desiatov B, Khurgin J, Shappir J and Levy U 2011 Locally Oxidized Silicon Surface-Plasmon Schottky Detector for Telecom Regime *Nano Lett.* **11** 2219–24

[34] Fedyanin D Y and Arsenin A V. 2011 Surface plasmon polariton amplification in metal-semiconductor structures *Opt. Express* **19** 12524

[35] Fedyanin D Y, Arsenin A V. and Chigrin D N 2010 Semiconductor Surface Plasmon Amplifier Based on a Schottky Barrier Diode *AIP Conference Proceedings* vol 1291 (American Institute of Physics) pp 112–4

[36] Li D and Ning C Z 2011 All-semiconductor active plasmonic system in mid-infrared wavelengths *Opt. Express* **19** 14594

[37] Soref R, Hendrickson J and Cleary J W 2012 Mid- to long-wavelength infrared plasmonic-photonics using heavily doped n-Ge/Ge and n-GeSn/GeSn heterostructures *Opt. Express* **20** 3814

[38] Fan P, Colombo C, Huang K C Y, Krogstrup P, Nygård J, Fontcuberta i Morral A and Brongersma M L 2012 An Electrically-Driven GaAs Nanowire Surface Plasmon Source *Nano Lett.* **12** 4943–7

[39] Vinnakota R K and Genov D A 2014 Terahertz Optoelectronics with Surface Plasmon Polariton Diode *Sci. Rep.* **4** 20–7

[40] Sze S M and Ng K K 2007 *Physics of semiconductor devices* (Wiley-Interscience)

[41] Varga B B 1965 Coupling of Plasmons to Polar Phonons in Degenerate Semiconductors *Phys. Rev.* **137** A1896–902

[42] Mooradian A and Wright G B 1966 Observation of the Interaction of Plasmons with Longitudinal Optical Phonons in GaAs *Phys. Rev. Lett.* **16** 999–1001

[43] Hase M, Nakashima S, Mizoguchi K, Harima H and Sakai K 1999 Ultrafast decay of coherent plasmon-phonon coupled modes in highly doped GaAs *Phys. Rev. B* **60** 16526–30

[44] Olson C G and Lynch D W 1969 Longitudinal-Optical-Phonon-Plasmon Coupling in GaAs *Phys. Rev.* **177** 1231–4

[45] Kuznetsov A V. and Stanton C J 1995 Coherent phonon oscillations in GaAs *Phys. Rev. B* **51** 7555–65

[46] Hu Z G, Rinzan M B M, Matsik S G, Perera A G U, Von Winckel G, Stintz A and Krishna S 2005 Optical characterizations of heavily doped p-type Al <sub x>x AsAl[sub x]Ga[sub 1−x]As and GaAs epitaxial films at terahertz frequencies *J. Appl. Phys.* **97** 093529

[47] Fehrenbacher M, Winnerl S, Schneider H, Döring J, Kehr S C, Eng L M, Huo Y, Schmidt O G,

Yao K, Liu Y and Helm M 2015 Plasmonic Superlensing in Doped GaAs *Nano Lett.* **15** 1057–61

[48] Sotoodeh M, Khalid A H and Rezazadeh A A 2000 Empirical low-field mobility model for III–V compounds applicable in device simulation codes J. Appl. Phys. **87** 2890

[49] Abernathy C R, Pearton S J, Caruso R, Ren F and Kovalchik J 1989 Ultrahigh doping of GaAs by carbon during metalorganic molecular beam epitaxy Appl. Phys. Lett. **55** 1750

[50] Levi A F J 1988 Scaling 'ballistic' heterojunction bipolar transistors Electron. Lett. **24** 1273 – 1275

[51] Collin R E 2001 *Foundations for microwave engineering* (IEEE Press)

[52] Pierret R F 1996 *Semiconductor Device Fundamentals* (Addison Wesley)

[53] Cunningham, S. L.; Maradudin, A. A.; Wallis R F 1974 Effect of a charge layer on the surface-plasmon-polariton dispersion curve *Phys. Rev. B* **10** 3342–55

[54] Kretschmann E and Raether H 1968 Radiative decay of non radiative surface plasmons excited by light Z. Naturf. A **23** 2135-2136

[55] Burke J J, Stegeman G I, and Tamir T 1986 Surface-polariton-like waves guided by thin, lossy metal films Phys. Rev. B **33** 5186

[56] Branch M A, Coleman T F and Li Y 1999 A Subspace, Interior, and Conjugate Gradient Method for Large-Scale Bound-Constrained Minimization Problems *SIAM J. Sci. Comput.* **21** 1–23